Chemical Engineering Journal Advances 13 (2023) 100438

Contents lists available at ScienceDirect

Chemical Engineering Journal Advances

journal homepage: www.sciencedirect.com/journal/chemical-engineering-journal-advances

Hydrodynamic behavior of a novel 3D-printed nature-inspired microreactor with a high length-to-surface ratio

Inmaculada García-López *, Vicente Ismael Águeda, Amalio Garrido-Escudero

Research Group Catalysis & Separation Processes (CYPS), Department of Chemical Engineering, Universidad Complutense de Madrid, Madrid, 28040, Spain

ARTICLE INFO

Keywords:
Microfluidics
Residence time distribution
Plug flow
CFD
3D printing
Mass transfer

ABSTRACT

Microreaction technology has experienced almost exponential growth in the last decades due to significant practical benefits when compared with conventional reactors. However, the predominantly laminar flow impedes the required mixing in some processes. A novel design inspired by differential growth organic shapes in nature for improving mass transfer in microreactors is proposed. Firstly, this geometry allowed an area utilization of 16,1% and 27,2% higher than conventional serpentine and spiral channels, with the same hydraulic diameter, which can be useful for surface contact processes as in electrochemical reactions. Secondly, the performance of the microreactor was analyzed in terms of fluid flow and residence time distribution (RTD) for Reynolds in a range from 1-100. The continuous bending in the differential growth shape geometry leads to the formation of secondary vortices while approaching to the plug flow regime for the studied flow rates. These results were obtained by numerical analysis executed with the software COMSOL Multiphysics by solving three-dimensional Navier-Stokes equations with a convection-diffusion model for the species concentration. The validation of the RTD numerical model was conducted in a one-body 3D-printed microreactor by injecting a pulse of rhodamine B in water and measuring the response with colorimetric techniques. These organic shapes open a window to further research in microfluidics, as its parametric design can be adapted to a wide variety of reaction conditions.

1. Introduction

Microfluidic systems are nowadays utilized in biochemical reactions, chemical synthesis, and biological activities. The smaller size of channels counts on significant advantages such as improved mixing and heat transfer, smaller sample sizes, safer operation, more controlled operation, etc.[1,2]. However, the flow condition in microchannels is mainly laminar, and the fluid tends to move in parallel flow streams with little disruption between the layers [3,4]. Mass transport occurs predominantly by molecular diffusion with a very low mixing efficiency, which is too slow for many applications where mixing is required to occur in short intervals [5]. In electrosynthesis, for instance, mass transport and electron transfer kinetics play a crucial role in the design of an adequate reactor [6]. Regarding mass transfer phenomena, a key challenge is still avoiding electrode polarization. It leads to zero concentration of reactants on the electrode, as they are immediately converted into products and not exchanged with fresh reagents. In this situation, mass transport limits the overall reaction rate [7]. Then, overcoming mass transfer limitations caused by the depletion boundary layer is critical to improving the reactants' conversion.

One strategy to disturb the laminar flow in microreactors is the introduction of chaotic advection. It consists of exciting the flow hydrodynamics generating spontaneous flow instabilities, enhanced by the separation of boundary layers and the induction of recirculating or secondary flows, split and recombination, recirculation, or transversal flow [8]. In electrochemical microreactors, one strategy to enhance mass transfer is the insertion of channeled flow fields or turbulence promoters in the fluid flow path near the electrodes. Concerning flow fields, some previously proposed designs include interdigitated flow fields (IFF) [9], serpentine, parallel, pin, [10], or spiral channels [11].

On the other hand, some fractal geometries have been proposed to promote mixing at the micro scale. A fractal is a geometric pattern that repeats itself under several levels of magnification, which produces more dense structures that can be described through mathematical expressions. There are a wide variety of fractal patterns in nature like trees, mountains, clouds, rivers, or blood vessels [12–14]. Some authors have previously proposed fractal geometries to promote mixing and heat transfer in microreactors: Koch snowflakes [15], Hilbert millireactors

* Corresponding author.
E-mail address: inmgarci@ucm.es (I. García-López).

https://doi.org/10.1016/j.ceja.2022.100438

Available online 21 December 2022

[16], or branched networks [17]. But to the best of our knowledge, differential growth shapes have not yet been tested in microfluidics. The behavior of these structures is similar to a wide variety of systems in nature that fold in on themselves, such as meandering rivers, plant growing, foliose lichen, or the space-filling behaviors of worms, snakes, intestines, or the human brain (Fig. 1a). These kinds of shapes can be convenient, for instance, in electrochemistry. Firstly, the intricate shape of the channels induces flow disturbance, promoting boundary layer disruption near the electrodes. Moreover, there exists a high electrode surface utilization, and very long reactor geometries can be adjusted on a small surface by proper "folding" of the tubing. This is a very interesting strategy to enhance the overall conversion in systems requiring high reaction times.

One of the main design parameters for microreactors is the residence time distribution (RTD), because poor uniformity in the distribution decreases the yield or selectivity of reaction products [18,19]. It is important to achieve a precise characterization of these novel flow fields in an electrochemical microreactor. It gives information about the axial dispersion in the channel, which affects the conversion of each fluid element and the overall conversion at the exit [20]. The measurement of the RTD can be done through a stimulus-response experiment by monitoring the change in concentration of a nonreactive tracer as it passes through the reactor. The selection of the tracer depends on the analysis method that will be used, which may be: radioactivity, thermal tracing, conductivity detection, or optical detection [21,22].

In addition, the accessibility to affordable and reliable 3D printing machines has benefited the field of electrochemical reactor design. 3D printing allows the manufacturing of complex flow fields for electrochemical cells in a fast, low-cost, and flexible way to test the hydrodynamic conditions of different designs. Besides, it facilitates the subsequent transition from prototype to bulk manufacturing [22,23]. The most widely used 3D printing techniques in microfluidics are selective laser sintering (SLS), fused deposition modeling (FDM), photopolymer inkjet printing, laminated object manufacturing (LOM), and stereolithography (SLA) [24]. Stereolithography (SLA) has appeared as one of the most promising alternatives for micro and millifluidics manufacturing due to its ability to fabricate objects with high accuracy and the possibility to employ a wide variety of materials. It is based on a polymerization process characterized by chemical cross-linking reactions, which are initiated by a UV light source in the range of 395 nm to 405 nm. A series of post-processing and additional curative processes are required. The selection of the most suitable 3D printing technology depends on the reactivity of reactants and products for a specific application [25,26].

In this work, the design of a differential growth shape channel algorithmically is proposed. Through numerical simulations, we determine the fluid flow characteristics in terms of velocity profile and pressure drop, as well as the RTD for quantifying its approach to ideal behavior. The validation of the RTD simulation results is based on the tracer injection technique in an SLA 3D printed prototype.

2. Materials and methods

2.1. Geometry modeling

At a high level, the differential growth process can be explained algorithmically as a line expansion growth assuming that we start with a user-defined, single, continuous path made up of points (referred to as nodes) connected by lines (called edges). The following guidelines apply in each iteration of the new curve formation: 1. each node will experience a mutual attraction force toward the adjacent nodes to whom it is attached; 2. each node will feel a mutual repulsion from all other nodes in its immediate vicinity; 3. each node will feel an alignment force toward the half of its neighbor nodes on a line as straight as possible [27].

Differential growth shapes can be generated through different modeling software. In this work, we used Rhinoceros 6 (McNeel & Assoc., USA), its extension Grasshopper, and specifically, the Kangaroo plug-in (Fig. 1b). It contains a series of algorithms that enable the simulation of some behaviors of real-world materials and objects [28]. To perform the simulation, the user must define the initial and the number of nodes in which an initial curve will be divided. The curve must be contained in a closed surface that will serve as the borders for the curve growth. Each segment of the curve gradually increases its length due to the physical collision of virtual spheres with a certain radius. Then, as the curve is not allowed to cross itself, the result is a curve uniformly filling the defined planar surface. Once the curve is generated, it is "baked" (a command in Grasshopper to reproduce the geometry in the Rhinoceros domain), thickened, and extruded with the desired channel width and height dimensions. Rhinoceros allows adapting the file format to export the geometries afterward to the computational fluid dynamics (CFD) software and to the 3D printing slicer.

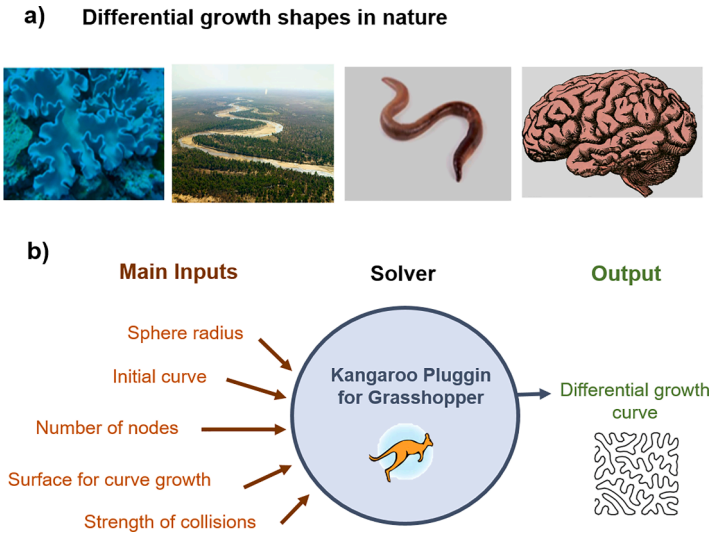

Fig. 1. Differential growth shapes. (a) Examples of folding geometries that follow differential growth in natural systems, from left to right: kale leaf, meander, worm, human brain (pictures retrieved from non-required attribution images bank). (b) Main input parameters to be connected to Kangaroo solver in the grasshopper algorithm. Differential growth shape curve as the output of the solver.

2.2. Formulation of numerical simulation

The numerical fluid flow analysis was carried out using the finite element method (FEM) software COMSOL Multiphysics 5.6, implementing the Laminar Flow and Transport of Diluted Species interfaces. These include the continuity (Eq. 1), Navier-Stokes (Eq. 2), and species convection-diffusion equations (Eq. 3), which are utilized to solve the flow field and component concentration distribution along the channel.

$$\nabla \cdot u = 0 \tag{1}$$

$$\rho\left(\frac{\partial u}{\partial t} + (u\cdot\nabla)u\right) + \nabla p + \mu\nabla^2 u = 0 \tag{2}$$

$$\frac{\partial c}{\partial t} = D\nabla^2 C - u\cdot\nabla c \tag{3}$$

where u is the fluid velocity (m s^{-1}), μ the dynamic viscosity (Pa s), ρ the density (kg m^{-3}), p the fluid pressure (Pa), c the concentration (mol m^{-3}) and D the diffusion coefficient (m^2 s^{-1}). Dynamic viscosity, density and diffusion coefficient values were set 0,001 Pa s, 10^3 kg m^{-3} and 4,26 10^{-6} cm^2 s^{-1} [29], respectively. The analyte is assumed diluted and thus ρ and μ do not depend on its concentration, and D is isotropic and constant. Uniform velocity was applied to the inlets and a constant zero-gauge pressure was established at the outlet. A no-slip condition was set at the microdevice channel walls. Reynolds number (Re) is an important non-dimensional number involved in the fluid flow study. It reflects the ratio of inertial with respect to viscous forces, and its definition appears in Eq. 4:

$$Re = \frac{\rho u D_h}{\mu} \tag{4}$$

Here, D_h is the hydraulic diameter of the channel (m). For the RTD assessment, a time-dependent study was designed. The age distribution of volume elements $E(t)$ exiting the reactor in a certain time was calculated by introducing a gaussian pulse. The function $E(t)$ indicates the probability that a fraction of the total amount entering the reactor at $t=0$ has left the reactor after the time t. For a pulse experiment, the $E(t)$ curve corresponds to Eq. 5:

$$E(t) = \frac{c(t)}{\int_0^\infty c(t)dt} \tag{5}$$

Where $c(t)$ represents the microreactor outlet concentration (mol m^{-3}) at time t. This value was obtained in COMSOL through the boundary probe option applied to the outlet boundary in the reactor. For facilitating the comparison among reactors of different sizes and throughputs, a dimensionless time is defined as in Eq. 6. It is also possible to refer the $E(t)$ curve to the non-dimensional time according to Eq. 7:

$$\theta = \frac{t}{t_{mean}} \tag{6}$$

$$E(\theta) = t_{mean}\cdot E(t) \tag{7}$$

Where t_{mean} is the average residence time in the reactor (s). It corresponds to the first moment of the distribution function, $E(t)$, as it appears in Eq. 8.

$$\mu_1 = t_{mean} = \int_0^\infty t\cdot E(t)dt \tag{8}$$

The variance of the distribution (σ^2) is obtained from the second moment of the distribution function, as in Eq. 9:

$$\sigma^2 = \mu_2 - \mu_1^2 = \int_0^\infty t^2\cdot E(t)dt - t_{mean}^2 \tag{9}$$

In its dimensionless form (σ_θ^2), the variance is defined as in Eq. 10:

$$\sigma_\theta^2 = \frac{\sigma_t^2}{t_{mean}^2} \tag{10}$$

Real reactors are often classified according to the degree of back mixing, which ranges between the ideal plug flow reactor (no back mixing) and the ideal CSTR (complete back mixing). The Bodenstein number (Bo) can be used to investigate the influence of dispersion (Eq. 11):

$$Bo = \frac{uL}{D_{ax}} \tag{11}$$

Where D_{ax} is the effective axial dispersion coefficient (m^2 s^{-1}), which comprises all effects of back mixing, such as the radial velocity profile in laminar flow, molecular diffusion, eddies, and vortices, and L is the reactor length (m). As the axial dispersion increases, the Bo decreases, and the RTD curve tends to widen. When Bo approaches zero, the axial dispersion is maximum, with a very wide RTD. This case corresponds to a perfectly mixed reactor. With increasing Bo number, the axial dispersion decreases, which can be even neglected at high Bo. In the latter scenario, an ideal plug flow reactor (PFR) can be assumed [30]. The most common threshold for this assumption is Bo=100 [31]. When there is low back mixing (Bo>100), the Bodenstein number can be expressed as (Eq. 12):

$$Bo = \frac{2}{\sigma_\theta^2} \tag{12}$$

In case the calculated Bo<100, the assumption of plug flow is not fulfilled. Then, Bo can be calculated as the expression proposed by [32] in Eq. 13:

$$Bo = \frac{1}{\sigma_\theta^2} + \sqrt{\left(\frac{1}{\sigma_\theta^2}\right)^2 + \frac{8}{\sigma_\theta^2}} \tag{13}$$

Considering Bo, the dispersion model is useful to predict the normalized E-curve, $E(\theta)$, for minor dispersion extents. It is suitable for Bo>100 [33] and can be expressed as in Eq. 14:

$$E(\theta) = \frac{1}{\sqrt{4\pi\left(\frac{1}{Bo}\right)}}\exp\left(-\frac{(1-\theta)^2}{4\left(\frac{1}{Bo}\right)}\right) \tag{14}$$

2.3. Experimental setup

The validation of the RTD numerical results was carried out in a 3D-printed microreactor. The fabrication process started by converting the 3D CAD geometry to a standard tessellation language (STL) file. By slicing the STL file, the 3D model is transformed into 2D information, which will be reproduced layer by layer by the 3D printer [25] (Fig. 2a). The microreactor was printed in a commercial and affordable SLA 3D printer (Anycubic Photon Mono, Shenzhen Anycubic Technology Co., Ltd.), optimized for 405 nm light, using a photopolymerizable liquid resin (Clear UV Resin, Shenzhen Anycubic Technology Co., Ltd.). The printing parameters were previously studied and adjusted, achieving better results with a layer height of 50 μm, exposure of 2 s, off-time of 0.5 s, bottom layer exposure of 40 s on 6 layers, a Z-lift distance and speed of 10 mm, and 2 mm/s and no anti-aliasing. Once the microreactor was printed, the excess of resin was removed with isopropyl alcohol, 99% wt, including the resin retained inside the microchannels. Next, the microreactors were cured by being exposed for 60 s to a 405 nm light source (Fig. 2b). For this particular channel length, the hydraulic diameter needed to be at least 1,5 mm for the acrylic resin extraction with a syringe. Otherwise, the resin remained trapped, plugging the channel.

The development of colorimetry methods using low-cost devices (i.e.

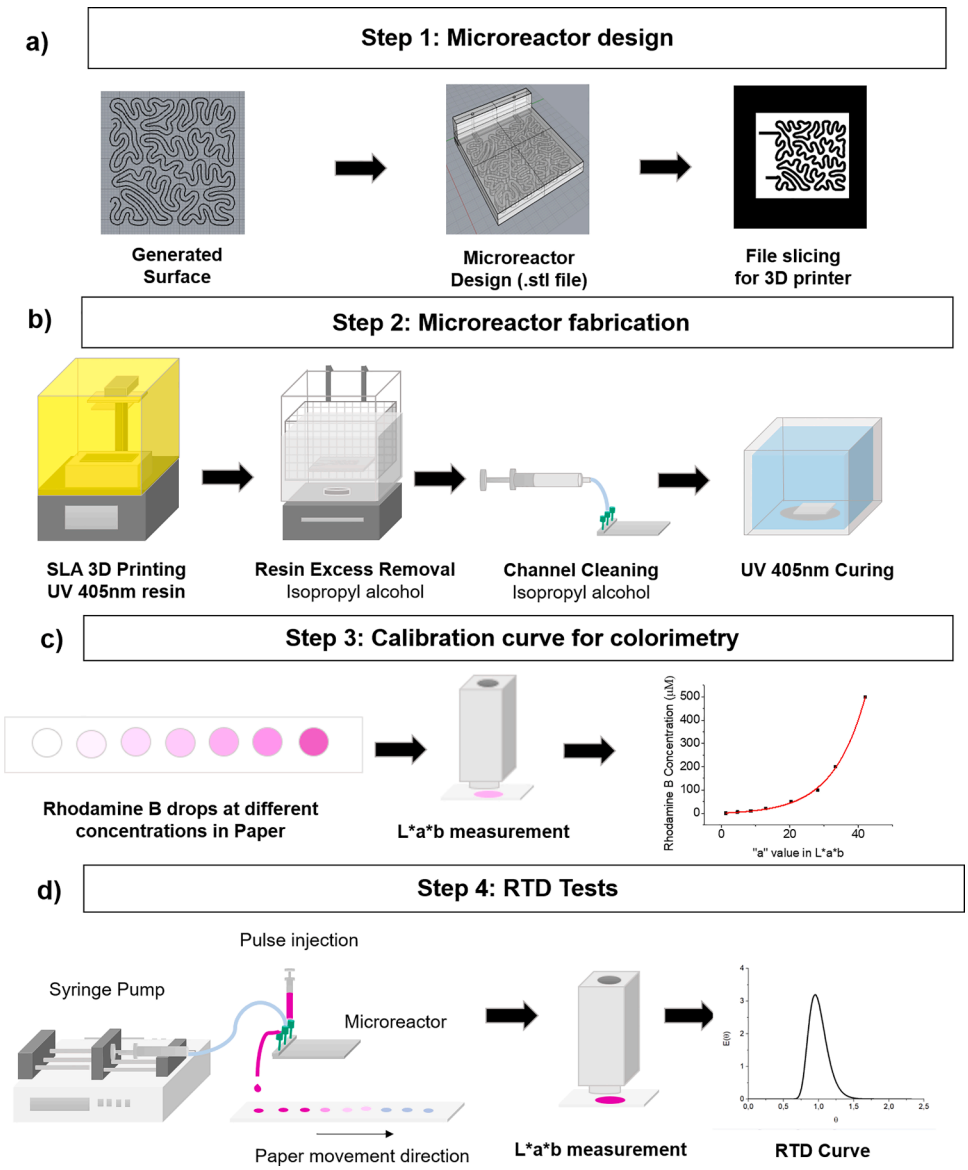

Fig. 2. Experimental procedure for RTD measurements. (a) Slicing of geometry in STL file to be translated into the 3D printer language. b) Microreactor 3D printing through the SLA technology, including the post-processing steps: resin cleaning with isopropyl alcohol and curing with a UV light emitting at 405nm. (c) Obtention of calibration curve for colorimetry by measuring the "a" parameter of different concentrations of Rhodamine B. (d) RTD tests performed by injecting a pulse of Rhodamine B and measuring the response by colorimetry.

smartphones) has been previously proposed in the literature in analytical chemistry research. For instance, Woolf et al. [34] proposed a protocol for monitoring the progression or the endpoint result of colorimetric reactions using a variety of space colors such as RGB or L*a*b or HSB. The image can be captured through smartphones or desktop scanners and processed with free software such as ImageJ, quantifying the analyst of interest. Other applications including colorimetric studies can be: chemical kinetics [35]; paper-based analysis of Fe^{2+} and Cu^{2+} [36]; prostate specific antigen (PSA) quantification with a smartphone [37], paper-based sensor for determination of mercury (Hg^{2+}) [38], quantification of commercial dyes in consumer goods [39] or determination of RTD in flexible fluoropolymer microcapillary films [40], among others.

In this study, the measurements of RTD were based on the paper-based colorimetric analysis of a pulse input of rhodamine B (LabChem Röttinger) in deionized water with a portable colorimeter (Linshang LS190). The use of handheld colorimeters has some advantages over image capturing with smartphones. It is possible to quantitatively determine the concentration of analytes in a manner that is independent of ambient lighting and does not require image post-processing. Before the tests on the microreactor, a calibration curve was constructed. Concentrations of rhodamine B ranging from 5 to 500 µM were prepared and three drops of solution per concentration were poured into white paper (46,5 g m^{-2} grammage) through a syringe. Then, the CIELAB color of each drop was analyzed by taking two-color measurements per drop of a certain concentration. The measurement of the background was also included. In this 3D color model, the *L*-values correspond to lightness, the *a*-values are related to redness and greenness, and the *b*-axis describes the color variation from blue to yellow. To perform the fitting, only *a* value was considered, as it was detected as the parameter with relevant variations among the samples (Fig. 2c). An exponential expression was fitted to the data, obtaining a value of R^2=0,9991.

For the RTD trials, a pulse of 0,1 ml a solution of rhodamine B (1 mM) was injected to the microreactor through a 1 ml syringe. The water was continuously fed through a 1/8" PEEK tubing using a syringe pump (KDS-100, KDScience). The experimental tests were carried out at *Re*=10 and *Re*=50, with inlet velocities of water of 0,006 and 0,03 m s^{-1}, respectively. The drops at the microreactor exit were deposited into tissue paper, with the same characteristics as in calibration to avoid changes in background color. The time between drops was considered for constructing the RTD curve. The color per drop was measured with the colorimeter, and the concentration of the tracer was calculated by substituting the *a* parameter of color into the calibrate curve (Fig. 2d).

3. Results and discussion

3.1. Geometry generation

Differential growth shapes offer higher surface utilization in comparison with other geometries previously employed in microfluidics. Fig. 3a represents the surface occupation of some frequent channel patterns (serpentine and spiral), and fractal geometry (Hilbert) in equal conditions: the channels are contained in a square of 40 × 40 mm and its hydraulic diameter is 1,5 mm in all cases. The designs have taken into account the minimum possible distance between two adjacent parts of the channel to be built by SLA 3D printing. In the case of the Hilbert curve, it is possible to continue increasing the channel length, but a higher recursion curve implies the channel overlapping for the given diameter of 1,5 mm, and it occurs with the differential growth curve. In summary, differential growth counts on 16,1%, 27,2%, and 29% more surface utilization than the serpentine, spiral, and Hilbert channels, respectively.

The number of initial curve divisions (number of initial nodes) has an impact on the final length of the channel, as increasing the number of divisions allows the curve to grow on more points, and therefore, increases the total length (Fig. 3b). For the same initial curve and growing surface, there is an increase in the final curve length concerning the initial nodes according to a linear fitting. This allows an adaption of the curve length, according to the reaction needs.

3.2. Independence mesh study

For the numerical analysis, a preliminary grid sensitivity analysis was executed at an inlet velocity of 0,03 m/s with four different grid systems. The number of triangular mesh elements of the 3D geometry varied from 0,37 10^6 to 3,34 10^6. The velocity profile was calculated in a cut line at the microreactor outlet, considering valid the differences in both average and maximum velocity lower than 2% between higher and lower meshes. The optimal mesh elements selected for further calculations from the test results was 1.24 10^6. The equations were solved using the generalized minimal residual method (GMRES) iterative solver. The convergence criteria employed in this numerical solution was the root-mean-square residual value of less than 10^{-6}.

3.3. Flow field: velocity and pressure drop

Fig. 4a represents the surface velocity in the channel cut plane at a height of 0,75 mm (center of the channel). In straight regions, the maximum velocity appears at the center of the channel (red region). Because of the tortuous nature of the proposed geometry, the laminar Poiseuille flow is subjected to centrifugal and centripetal forces and the parabolic profile is disrupted. The highest velocity is displaced towards

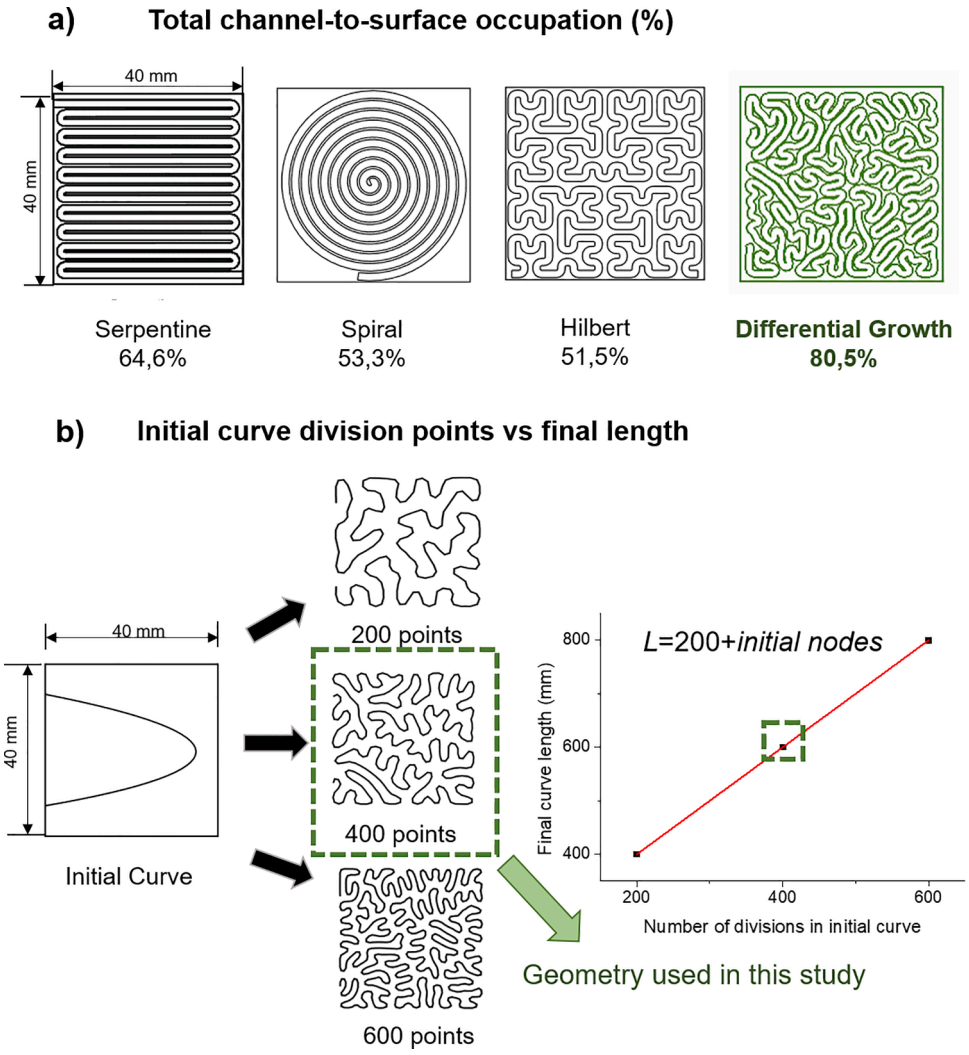

Fig. 3. Geometry characteristics: (a) Comparison of surface occupation in a 40 × 40 mm square space with hydraulic diameters of 1,5 mm. (b) Influence of the number of node divisions of the initial curve in the final curve length, keeping the rest of the algorithm parameters constant.

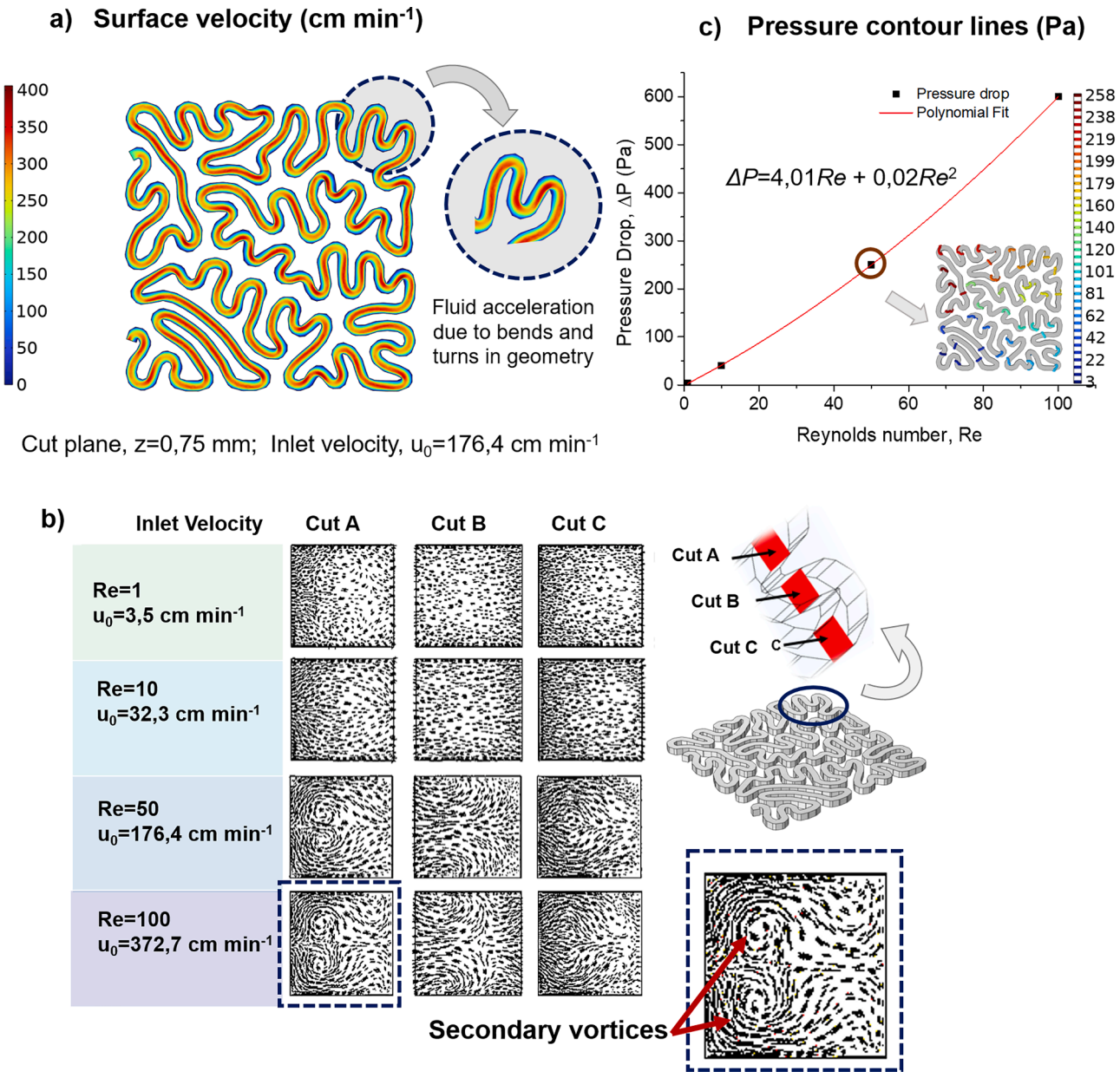

Fig. 4. (a) Surface velocity in the XY cut plane at z=0,75 mm (center of the channel) at a Re=50. (b) Normalized arrow velocity components at different cross-sectional cut planes and Re number. (c) Pressure drop at different Re.

the concave side of the channel, producing a sharp velocity and pressure gradient with respect to the convex side. To balance this pressure gradient, there occurs secondary flows from the concave to the convex wall of the channel [41–43]. These flows are characterized by the presence of counter-rotating vortices, associated to the Dean number (*De*) as in Eq. 15 [44]:

$$De = Re\sqrt{\frac{D_h}{R_c}} \tag{15}$$

Here R_c is the curvature radius of the channel (m). When the curvature of the channel decreases, there is an increase in *De*, due to higher centrifugal forces. To visualize the existence of secondary flows inside the channel, the normalized velocity vectors were represented at three different cross-sectional planes depending on Re (Fig. 4b). As derived from the numerical results, at the lowest fluid velocity (*Re*=1), the fluid tended to flow in parallel streams and no evident secondary flows are observed. When *Re* increases, the recirculation near the outer channel wall became more pronounced, developing two primary Dean vortices. At *Re*=100, the primary Dean vortices are split into two small counter-rotating vectors at the opposite wall side.

It is important to analyze pressure losses for the differential growth geometry, as it related to the pumping pressure needed at the inlet of the microreactor for the liquid to flow inside it. The mechanical energy in laminar flow in a microreactor is dissipated mainly by the fluid wall friction and the chaotic secondary flow vortex structures caused by the pressure gradient. If the bend curvature is strong, the adverse pressure gradient near the wall produces flow separation at these points, which could provoke a large increase in pressure losses. The magnitude of the pressure loss is a function of friction and momentum exchanges, which are in turn dependent on bend angle, the curvature ratio, and the *Re* [45]. Because of higher bends and turns in the differential growth geometry, the pressure drop in these systems may result higher in comparison to other simpler, conventional geometries such as serpentine, which counts on less fluid re-directions. However, the pressure drop in differential growth structure is manageable for microfluidics. In fact, it

is several orders of magnitude lower than other mixing structures with similar cross-section, *Re* and channel lengths [46]. On the other hand, pressure losses increase for higher flow rates because of increased wall frictions and stronger secondary vortices. This prediction is evidenced in Fig. 4c., where pressure drop increases with an increase in the Reynolds number according to a second-degree polynomial equation.

3.4. RTD studies

Non-dimensional RTD was studied for Re ranging from 1 to 100 (Fig. 5a). The curve maximum appears in the vicinity of non-dimensional time, θ=1. The laminar flow profile is broken due to molecular diffusion and secondary flows, which improves mixing in the radial direction. The curve (θ) is not totally symmetrical, as the maximum of (θ) tends to be slightly displaced to θ<1. This implies that a portion of fluid advances faster than the rest due to the presence of preferential paths (by-passing). Moreover, as the fluid velocity increases, the (θ) tends to flatten. The fluid acceleration leads to the presence of dead zones, inducing a larger concentration tail in the RTD curve. In contrast, at higher flow rates, the formation of secondary vortices is considerably superior, as previously seen in Fig. 4b. Achieving plug-flow regime may be important to perform accurate kinetic in applications such as cell culture, drug discovery, or organs-on-chip. Other applications such as electrochemical microreactors may prioritize the disturbance of the concentration boundary layers near the electrodes, and therefore, it might be beneficial to operate at higher *Re*.

Bodenstein number (*Bo*) is related to the axial dispersion coefficient in an inverse way. For a given channel diameter, the axial dispersion increases with the fluid velocity, and so with *Re*. Then, *Bo* decreases with an increase in flow rate as shown in Fig. 5a. This result is in agreement with [21], who studied the influence of flow rate on dispersion coefficient in a rectangular, wavy microchannel. Nevertheless, for all proposed Re, the Bo number is higher than 100 (Fig. 5b), which is in principle the limit to consider low dispersion and assume plug flow in the microreactor.

Fig. 5c shows the comparison of RTD curves for simulated, fitted to the dispersion model, and experimental for *Re*=10 and *Re*=50. The fitted dispersion model agrees with the simulation results. The differences between numerical simulation and experimental results may be explained because the dimensions of the fabricated channel differed slightly from the reference dimensions. Some wall roughness was induced in the fabrication process as the cleaning with isopropyl alcohol is difficult and does not remove totally the acrylic resin, as it has a high viscosity. Surface roughness can have a substantial impact on fluid dynamics by causing perturbations in the velocity profile that affect surface drag, and turbulent mixing [47]. Besides, the walls in the simulation were assumed to have the no-slip condition in the numerical calculations, which might contribute to the differences between the numerical results and experimental data. It is suggested to conduct further experiments inducing rugosity in the simulation. Another possible cause of differences between the simulation and experimental results is due to the interaction of the rhodamine B with the microreactor construction material. Small amounts of the tracer may have been retained into the walls, which affects to the outlet tracer concentration.

As demonstrated, differential growth geometries count on higher surface utilization with respect to other previously proposed shapes. They can be useful to perform reactions requiring long residence times in a very compact surface. In the case of electrochemical microreactors,

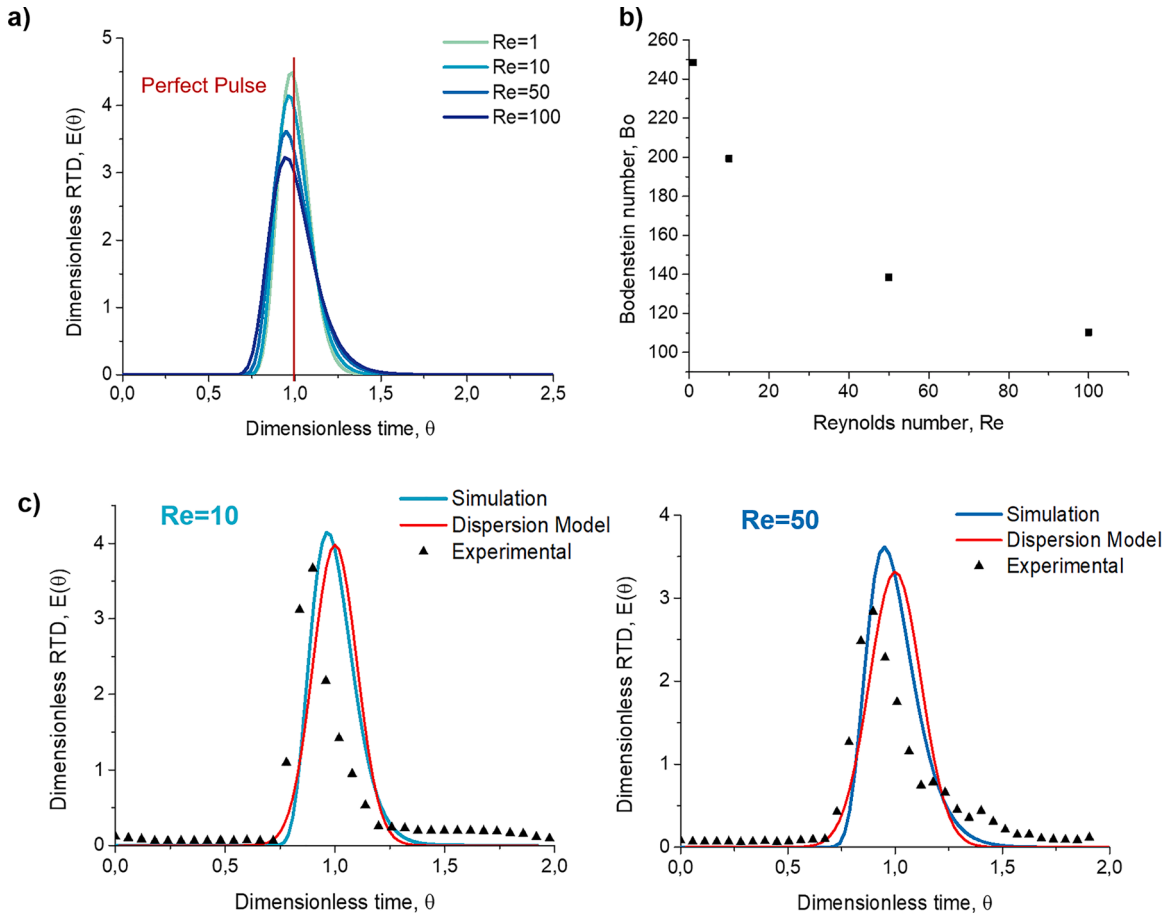

Fig. 5. RTD analysis: a) RTD simulation results: non-dimensional E(Θ) curve for different Re; b) Bodenstein number at different Re from simulation results (c) Comparison of non-dimensional E(Θ): numerical, experimental (measured by colorimetry) and fitting of the dispersion model for Re=10 and Re=50.

this minimizes the surface of electrode needed. Besides, the bends and turns in the channel promote the formation of secondary vortices that promote cross-sectional mixing of the fluid. A narrow RTD ensures the plug flow characteristic of this novel design in the studied flow range.

4. Conclusions

A novel geometry for microchannels inspired by bending nature systems has been presented. This geometry offers higher surface utilization in comparison to conventional channel designs, which can be useful for a wide number of surface reaction. The microreactor was characterized hydrodynamically by a numerical study performed with COMSOL Multiphysics, by solving the Navier-Stokes together with the convection-diffusion. The velocity vector analysis exhibited the formation of secondary flows at $Re>10$, which promotes micromixing in the channel cross-section. This disruption of the laminar flow leads to turbulence at a cost of an increased pressure loss, comparable with other mixing structures utilized in microfluidics. The RTD curves were confirmed experimentally by a 3D printed microreactor through the tracer injection technique at different *Re* numbers. The shape of the curve in the COMSOL simulation tended to plug flow regime with small deviation due to the fluid acceleration and dead volumes, mainly. In comparison with the numerical results, the experimental results differed slightly due to possible geometric variations during the microreactor fabrication, the presence of dead volumes or the loss of a small amount of tracer due to its interaction walls. The algorithmic differential growth system has potential applications in fields like organic electrosynthesis, requiring high surface contact and long residence times to achieve higher conversion. It represents an opportunity for future research, relative to the analysis of mass transport performance and current distribution under the influence of electric fields.

Funding source

The authors declare that they have not received any financial support for conducting the research nor the preparation of the article.

Declaration of Competing Interest

The authors declare that they have no known competing financial interests or personal relationships that could have appeared to influence the work reported in this paper.

References

[1] H. Abdulla Yusuf, S.M.Z. Hossain, S. Aloraibi, N.J. Alzaabi, M.A. Alfayhani, H. J. Almedfaie, Fabrication of novel microreactors in-house and their performance analysis via continuous production of biodiesel, Chem. Eng. Process. - Process Intensif. 172 (2022), 108792, https://doi.org/10.1016/j.cep.2022.108792.
[2] A.A. Bojang, H.-S. Wu, Design, fundamental principles of fabrication and applications of microreactors, Processes 8 (2020) 891, https://doi.org/10.3390/pr8080891.
[3] G. Cai, L. Xue, H. Zhang, J. Lin, A Review on Micromixers, Micromachines 8 (2017) 274, https://doi.org/10.3390/mi8090274.
[4] C.-Y. Lee, C.-L. Chang, Y.-N. Wang, L.-M. Fu, Microfluidic mixing: a review, Int. J. Mol. Sci. 12 (2011) 3263–3287, https://doi.org/10.3390/ijms12053263.
[5] J.T. Adeosun, A. Lawal, Mass transfer enhancement in microchannel reactors by reorientation of fluid interfaces and stretching, Sens. Actuators B Chem. 110 (2005) 101–111, https://doi.org/10.1016/j.snb.2005.01.016.
[6] S.C. Perry, C. Ponce de León, F.C. Walsh, Review—the design, performance and continuing development of electrochemical reactors for clean electrosynthesis, J. Electrochem. Soc. 167 (2020), 155525, https://doi.org/10.1149/1945-7111/abc58e.
[7] T. Subbaiah, S.C. Das, R.P. Das, Mass transfer rates in an electrochemical cell, Hydrometallurgy 33 (1993) 153–163, https://doi.org/10.1016/0304-386X(93)90011-2.
[8] A. Osorio-Nesme, A. Delgado, Flow characterization in periodic microchannels containing asymmetric grooves, Fluid Dyn. Res. 49 (2017), 055502, https://doi.org/10.1088/1873-7005/aa7a35.
[9] R. Gundlapalli, S. Jayanti, Performance characteristics of several variants of interdigitated flow fields for flow battery applications, J. Power Sources. 467 (2020), 228225, https://doi.org/10.1016/j.jpowsour.2020.228225.
[10] H. Liu, P. Li, D. Juarez-Robles, K. Wang, A. Hernandez-Guerrero, Experimental study and comparison of various designs of gas flow fields to PEM fuel cells and cell stack performance, Front. Energy Res. 2 (2014). https://www.frontiersin.org/articles/10.3389/fenrg.2014.00002 (accessed October 2, 2022).
[11] R.A. Green, R.C.D. Brown, D. Pletcher, B. Harji, An extended channel length microflow electrolysis cell for convenient laboratory synthesis, Electrochem. Commun. 73 (2016) 63–66, https://doi.org/10.1016/j.elecom.2016.11.004.
[12] J. Harris, Fractal architecture: organic design philosophy in theory and practice, UNM Press, 2012.
[13] K.E. Robles, N.A. Liaw, R.P. Taylor, D.A. Baldwin, M.E. Sereno, A shared fractal aesthetic across development, Humanit. Soc. Sci. Commun. 7 (2020) 1–8.
[14] X. Chen, T. Li, J. Shen, Z. Hu, Fractal design of microfluidics and nanofluidics—a review, Chemom. Intell. Lab. Syst. 155 (2016) 19–25, https://doi.org/10.1016/j.chemolab.2016.04.003.
[15] A. Adrover, Laminar convective heat transfer across fractal boundaries, EPL Europhys. Lett. 90 (2010) 14002, https://doi.org/10.1209/0295-5075/90/14002.
[16] C.A. Grande, Compact reactor architectures designed with fractals, React. Chem. Eng. 6 (2021) 1448–1453, https://doi.org/10.1039/D1RE00107H.
[17] J.-H. Huang, J. Kim, N. Agrawal, A.P. Sudarsan, J.E. Maxim, A. Jayaraman, V. M. Ugaz, Rapid fabrication of bio-inspired 3D microfluidic vascular networks, Adv. Mater. 21 (2009) 3567–3571, https://doi.org/10.1002/adma.200900584.
[18] M. Günther, S. Schneider, J. Wagner, R. Gorges, Th. Henkel, M. Kielpinski, J. Albert, R. Bierbaum, J.M. Köhler, Characterisation of residence time and residence time distribution in chip reactors with modular arrangements by integrated optical detection, Chem. Eng. J. 101 (2004) 373–378, https://doi.org/10.1016/j.cej.2003.10.019.
[19] J.L. da Silva, H.S. Santana, Residence time distribution in reactive and non-reactive flow systems in micro and millidevices, Chem. Eng. Sci. 248 (2022), 117163, https://doi.org/10.1016/j.ces.2021.117163.
[20] S.R.L. Gobert, S. Kuhn, L. Braeken, L.C.J. Thomassen, Characterization of milli- and microflow reactors: mixing efficiency and residence time distribution, Org. Process Res. Dev. 21 (2017) 531–542, https://doi.org/10.1021/acs.oprd.6b00359.
[21] M. Moreau, N. Di Miceli Raimondi, N.Le Sauze, C. Gourdon, M. Cabassud, A new numerical method for axial dispersion characterization in microreactors, Chem. Eng. Sci. 168 (2017) 178–188, https://doi.org/10.1016/j.ces.2017.04.040.
[22] A.V. Nielsen, M.J. Beauchamp, G.P. Nordin, A.T. Woolley, 3D printed microfluidics, Annu. Rev. Anal. Chem. Palo Alto Calif. 13 (2020) 45–65, https://doi.org/10.1146/annurev-anchem-091619-102649.
[23] H.S. Santana, A.C. Rodrigues, M.G.M. Lopes, F.N. Russo, J.L. Silva, O.P. Taranto, 3D printed millireactors for process intensification, Chin. J. Chem. Eng. 28 (2020) 180–190, https://doi.org/10.1016/j.cjche.2018.12.013.
[24] A.K. Au, W. Lee, A. Folch, Mail-order microfluidics: evaluation of stereolithography for the production of microfluidic devices, Lab. Chip. 14 (2014) 1294–1301, https://doi.org/10.1039/C3LC51360B.
[25] J. Huang, Q. Qin, J. Wang, A review of stereolithography: processes and systems, Processes 8 (2020) 1138, https://doi.org/10.3390/pr8091138.
[26] M.M. Sarafraz, F.C. Christo, Thermal and flow characteristics of liquid flow in a 3D-printed micro-reactor: a numerical and experimental study, Appl. Therm. Eng. 199 (2021), 117531, https://doi.org/10.1016/j.applthermaleng.2021.117531.
[27] Webb, J.. Exploring 2D differential growth with JavaScript. https://medium.com/@jason.webb/2d-differential-growth-in-js-1843fd51b0ce (accessed October 3, 2022).
[28] D. Piker, Kangaroo: form finding with computational physics, Archit. Des. 83 (2013) 136–137, https://doi.org/10.1002/ad.1569.
[29] P.-O. Gendron, F. Avaltroni, K.J. Wilkinson, Diffusion coefficients of several rhodamine derivatives as determined by pulsed field gradient–nuclear magnetic resonance and fluorescence correlation spectroscopy, J. Fluoresc. 18 (2008) 1093–1101, https://doi.org/10.1007/s10895-008-0357-7.
[30] K.D. Nagy, B. Shen, T.F. Jamison, K.F. Jensen, Mixing and dispersion in small-scale flow systems, Org. Process Res. Dev. 16 (2012) 976–981, https://doi.org/10.1021/op200349f.
[31] O. Levenspiel, Chem. Reaction Eng. (1972), https://doi.org/10.1021/ie990488g.
[32] O. Levenspiel, The dispersion model, in: O. Levenspiel (Ed.), Tracer Technol. Model. Flow Fluids, Springer, New York, NY, 2012, pp. 47–70, https://doi.org/10.1007/978-1-4419-8074-8_6.
[33] J.A. Conesa, Chemical Reactor Design: Mathematical Modeling and Applications, John Wiley & Sons, 2019.
[34] M.S. Woolf, L.M. Dignan, A.T. Scott, J.P. Landers, Digital postprocessing and image segmentation for objective analysis of colorimetric reactions, Nat. Protoc. 16 (2021) 218–238.
[35] M. Dangkulwanich, K. Kongnithigarn, N. Aurnoppakhun, Colorimetric measurements of amylase activity: improved accuracy and efficiency with a smartphone, J. Chem. Educ. 95 (2018) 141–145, https://doi.org/10.1021/acs.jchemed.7b00468.
[36] M.T. Koesdjojo, S. Pengpumkiat, Y. Wu, A. Boonloed, D. Huynh, T.P. Remcho, V. T. Remcho, Cost effective paper-based colorimetric microfluidic devices and mobile phone camera readers for the classroom, J. Chem. Educ. 92 (2015) 737–741, https://doi.org/10.1021/ed500401d.
[37] A.I. Barbosa, P. Gehlot, K. Sidapra, A.D. Edwards, N.M. Reis, Portable smartphone quantitation of prostate specific antigen (PSA) in a fluoropolymer microfluidic device, Biosens. Bioelectron. 70 (2015) 5–14, https://doi.org/10.1016/j.bios.2015.03.006.
[38] K.Shrivas Monisha, T. Kant, S. Patel, R. Devi, N.S. Dahariya, S. Pervez, M.K. Deb, M.K. Rai, J. Rai, Inkjet-printed paper-based colorimetric sensor coupled with smartphone for determination of mercury (Hg2+), J. Hazard. Mater. 414 (2021), 125440, https://doi.org/10.1016/j.jhazmat.2021.125440.

[39] J.F. Destino, K. Cunningham, At-home colorimetric and absorbance-based analyses: an opportunity for inquiry-based, laboratory-style learning, J. Chem. Educ. 97 (2020) 2960–2966, https://doi.org/10.1021/acs.jchemed.0c00604.
[40] K.K. Gill, Z. Liu, N.M. Reis, Fast prototyping using 3D printed templates and flexible fluoropolymer microcapillary films offers enhanced micromixing in immobilised (bio)catalytic reactions, Chem. Eng. J. 429 (2022), 132266, https://doi.org/10.1016/j.cej.2021.132266.
[41] H. Fellouah, C. Castelain, A. Ould El Moctar, H. Peerhossaini, A criterion for detection of the onset of Dean instability in Newtonian fluids, Eur. J. Mech. - BFluids. 25 (2006) 505–531, https://doi.org/10.1016/j.euromechflu.2005.11.002.
[42] N. Nivedita, P. Ligrani, I. Papautsky, Dean flow dynamics in low-aspect ratio spiral microchannels, Sci. Rep. 7 (2017) 44072, https://doi.org/10.1038/srep44072.
[43] Z. Anxionnaz-Minvielle, M. Cabassud, C. Gourdon, P. Tochon, Influence of the meandering channel geometry on the thermo-hydraulic performances of an intensified heat exchanger/reactor, Chem. Eng. Process. Process Intensif. 73 (2013) 67–80, https://doi.org/10.1016/j.cep.2013.06.012.
[44] W.R. Dean, J. Hurst, Note on the motion of fluid in a curved pipe, Philos, Mag. Ser. 7 (1927) 208.
[45] S. Jayanti, Bends, Flow and Pressure Drop in, Begel House Inc., 2011, https://doi.org/10.1615/AtoZ.b.bends_flow_and_pressure_drop_in.
[46] C.P. Holvey, D.M. Roberge, M. Gottsponer, N. Kockmann, A. Macchi, Pressure drop and mixing in single phase microreactors: Simplified designs of micromixers, Chem. Eng. Process. Process Intensif. 50 (2011) 1069–1075, https://doi.org/10.1016/j.cep.2011.05.016.
[47] M. Kadivar, D. Tormey, G. McGranaghan, A review on turbulent flow over rough surfaces: fundamentals and theories, Int. J. Thermofluids. 10 (2021), 100077, https://doi.org/10.1016/j.ijft.2021.100077.